

# The Method of Failure Paths for Reduced-Order Computational Homogenization

Paul Sparks and Caglar Oskay\*

Department of Civil and Environmental Engineering  
Vanderbilt University  
Nashville, TN, 37235

## Abstract

We present a new eigendeformation-based reduced order homogenization approach for simulating progressive degradation and failure in brittle composite materials. A new reduced model basis construction strategy is proposed, where the bases are based on numerically calculated “failure paths” within the material microstructure subjected to a pre-selected set of load configurations. The failure paths are allowed to overlap, leading to a slight deviation from orthonormality of the basis functions of the reduced order model. In order to alleviate the spurious post failure residual stresses, we propose a new hierarchical failure path update approach, where the influence functions are adaptively updated to incorporate compatible eigenstrains as microstructural failures are detected. The reduced order modeling approach is verified against particulate composite microstructures with ordered and random configurations. The proposed approach leads to significant improvements in accuracy, while maintaining a low model order.

*Keywords:* damage mechanics, reduced order homogenization, multiscale modeling, heterogeneous materials.

## 1 Introduction

Computational homogenization (CH) has emerged as a powerful tool for modeling the mechanical behavior of structures made of composite and other heterogeneous materials. The CH method is based on the mathematical homogenization theory [2, 5, 44, 47] and has been extensively used to address the elastic, inelastic, viscous and damage behavior (e.g., [26, 21, 45, 35]), geometric nonlinearities (e.g., [20, 30, 49]) and multiphysics response (e.g., [42, 48]). Recently, the CH method has also been extended to model fracture phenomena [32, 4, 38].

One of the main challenges before CH is the computational complexity of solving boundary value problems (BVPs) at two (or more) scales. Major progress in reducing the computational

---

\*Corresponding Author: VU Station B#351831, 2301 Vanderbilt Place, Nashville, TN 37235. Email: caglar.oskay@vanderbilt.edu

cost of the multiscale methods has been made through the introduction of reduced order modeling (ROM) approaches, including the generalized method of cells [1], the fast Fourier transform [36], the network approximation method [6], the R3M method [52], the proper generalized decomposition (PGD) [31, 12, 14], the nonlinear manifold-based ROM [7], among others. Many of the ROM approaches rely on the approximation of the fine scale response based on a small number of basis functions, typically far smaller than the standard (e.g., finite element) basis required to evaluate the fully-resolved fine scale problem discretizing the material heterogeneity. The central question of the reduced basis representation is how to choose the appropriate basis functions to represent the fine scale response.

Proper orthogonal decomposition (POD) has also been used to efficiently solve nonlinear multiscale problems [52, 11, 27]. The key feature of POD is that the optimality of the reduced basis in approximating the fully resolved (fine scale) system is ensured in the sense of a certain norm [37]. A challenge associated with this approach is that the optimality is often ensured with respect to a global norm, which may not always be feasible for analysis of problems involving localized failure events. Eigendeformation-based reduced order homogenization method (EHM) is an alternative model order reduction approach for problems that involve nonlinear material behavior [40, 15]. EHM is based on the transformation field analysis (TFA) originally proposed by Dvorak and coworkers [18, 19] and have been applied to study composite behavior under a range of loading conditions [39, 51, 28, 17, 10, 8, 9] and recently extended to model polycrystalline microstructures [53]. Similar to POD or PGD-based approaches, the model order reduction is achieved through the application of the principle of separation of variables (i.e., with respect to time and space), along with the finite sum decomposition:

$$f(\mathbf{y}, t) \approx \hat{f}(\mathbf{y}, t) = \sum_{\alpha=1}^n N^{(\alpha)}(\mathbf{y}) f^{(\alpha)}(t) \quad (1)$$

In contrast to the POD and PGD approaches, in which the decomposition is typically applied to the cardinal response fields (e.g.,  $f$  the displacement field), EHM relies on the decomposition of the gradient fields (i.e.,  $f$  the stress or strain field). EHM also accounts for the progressive decohesion along the interfaces of the heterogeneous material constituents [40, 41]. The current manuscript focuses on addressing two key challenges associated with EHM: (1) identification of a low-order reduced basis that accurately describes the progressive failure in a heterogeneous material microstructure; and (2) efficient alleviation of spurious post failure residual stresses observed in EHM model predictions.

The accuracy and the efficiency of an EHM model is controlled by the selection of the number (i.e.,  $n$ ) and shape (i.e.,  $N^{(\alpha)}$ ) of the basis functions. Basis functions that are piecewise constant [16] and nonlinear [34, 24] over the material microstructure have been previously

proposed. The particular forms of the basis functions could be chosen a-priori, using microstructure simulations subjected to (typically) simple loading histories, or adaptively through hierarchically updating the model order and basis functions as a function of the deformation state. While accurate, implementation and use of adaptive model update is computationally more complex. The authors previously performed an optimization-based identification of the optimal EHM model through evolutionary optimization [46]. While this approach is computationally costly, it provides a benchmark for accuracy assessment for ROM selection algorithms.

When low-order EHM models are employed to characterize failure in heterogeneous materials, a stress-locking phenomenon is observed [15, 23]. This locking phenomenon is associated with a residual stiffness after the onset of strain softening, the effect of which may be significant for some microstructural configurations [40, 23]. Crouch and Oskay [15] proposed the concept of shadow modeling, in which the post-failure stresses are computed based on a high order model, whereas the damage coefficients are evaluated using a low-order model to maintain low computational cost. In the context of unidirectional composites, Fish et al. [23] applied the idea of compatible eigenstrains to EHM (following the notion originally proposed by Furuhashi and Mura [25]) that eliminates load transfer to the inclusion phase upon failure, thereby eliminating the spurious post-failure stresses.

This manuscript presents a new EHM approach for simulating progressive degradation and failure in composite materials. A new reduced basis selection strategy is proposed, in which the basis functions are constructed based on the numerically calculated “failure paths” within the material microstructure under a pre-selected set of load configurations admissible by the homogenization theory. In the proposed methodology, the failure paths are allowed to overlap, leading to a slight deviation from orthonormality of the basis functions of the reduced order model. In order to alleviate the spurious post failure residual stresses, we propose a new hierarchical failure path update approach, where the influence functions are adaptively updated to incorporate numerically-computed compatible eigenstrains as microstructural failures are detected. The proposed reduced order modeling framework is verified against particulate composite microstructures with ordered and random configurations. The proposed reduced order modeling approach leads to significant improvements in accuracy, while maintaining a low model order.

The remainder of this manuscript is organized as follows: The problem of progressive failure in a composite material and the multiscale setting are stated in Section 2. The macroscale and microscale boundary value problems in the context of the EHM are described in Section 3. In Section 4, the method of failure paths and the reduced basis identification strategy are presented. Section 5 introduces the formulation to alleviate post-failure residual stresses. Numerical examples and assessment of model validity is provided in Section 6. Section 7

discusses the conclusions and future research directions.

## 2 Problem statement and multiscale setting

Consider a heterogeneous structure that occupies  $\Omega \subset \mathbb{R}^{n_{\text{sd}}}$ , where  $n_{\text{sd}}$  is the number of space dimensions. The equations governing the progressive failure of the heterogeneous structure are ( $\mathbf{x} \in \Omega$  and  $t \in [0, t_0]$ ):

$$\sigma_{ij,j}^{\zeta}(\mathbf{x}, t) + b_i^{\zeta}(\mathbf{x}, t) = 0 \quad (2)$$

$$\sigma_{ij}^{\zeta}(\mathbf{x}, t) = L_{ijkl}^{\zeta}(\mathbf{x})(\varepsilon_{kl}^{\zeta}(\mathbf{x}, t) - \mu_{kl}^{\zeta}(\mathbf{x}, t)) \equiv [1 - \omega^{\zeta}(\mathbf{x}, t)]L_{ijkl}^{\zeta}(\mathbf{x})\varepsilon_{kl}^{\zeta}(\mathbf{x}, t) \quad (3)$$

$$\varepsilon_{ij}^{\zeta}(\mathbf{x}, t) = u_{(i,j)}^{\zeta}(\mathbf{x}, t) \equiv \frac{1}{2}(u_{i,j}^{\zeta} + u_{j,i}^{\zeta}) \quad (4)$$

$$\dot{\omega}^{\zeta} = \hat{\omega}^{\zeta}(\sigma_{ij}^{\zeta}, \epsilon_{ij}^{\zeta}, \mathbf{s}_{ij}^{\zeta}) \quad (5)$$

where,  $\mathbf{u}^{\zeta}$  denotes displacement,  $\boldsymbol{\sigma}^{\zeta}$  the Cauchy stress,  $\mathbf{b}^{\zeta}$  the body force and  $\boldsymbol{\varepsilon}^{\zeta}$  the total strain, and  $\boldsymbol{\mu}^{\zeta}$  is the damage-induced inelastic strain. A superscript  $\zeta$  indicates the oscillatory behavior of the response fields due to the local microstructural heterogeneities. A subscript comma denotes spatial differentiation, parentheses in the subscript denotes a symmetric differentiation. The tensor of elastic moduli,  $\mathbf{L}^{\zeta}$  is taken to be symmetric and strongly elliptic. The progressive failure at a material point within the material microstructure is idealized using continuum damage mechanics. The state of damage at the material point is described by the scalar damage variable  $\omega \in [0, 1)$  with  $\omega = 0$  and  $\omega \rightarrow 1$  respectively indicating the states of no damage and complete loss of load carrying capacity.  $t_0$  denotes the end of the observation window. The evolution of the damage variable (Eq. 5) is provided in functional form and an explicit definition in the context of integral-type nonlocal damage formulation is presented in Section 3. The boundary conditions are:

$$u_i^{\zeta}(\mathbf{x}, t) = \hat{u}_i(\mathbf{x}, t) \quad \mathbf{x} \in \partial\Omega^u, \quad t \in [0, t_0] \quad (6)$$

$$\sigma_{ij}^{\zeta}(\mathbf{x}, t)n_j = \hat{t}_i(\mathbf{x}, t) \quad \mathbf{x} \in \partial\Omega^t, \quad t \in [0, t_0] \quad (7)$$

in which  $\hat{\mathbf{u}}(\mathbf{x})$  and  $\hat{\mathbf{t}}(\mathbf{x})$  are the prescribed displacement and tractions on the boundaries  $\partial\Omega^u$  and  $\partial\Omega^t$ , where  $\partial\Omega^u \cup \partial\Omega^t = \partial\Omega$  and  $\partial\Omega^u \cap \partial\Omega^t = \emptyset$ .  $\mathbf{n}$  is the unit normal to  $\partial\Omega^t$ .

The heterogeneous structure is formed by repetition of a locally periodic microstructure, which consists of  $c \geq 2$  constituent phases. The canonical domain of the microstructure is denoted as  $\Theta \subset \mathbb{R}^{n_{\text{sd}}}$ . The macro- and the microstructure domains are parameterized by the position vectors,  $\mathbf{x}$  and  $\mathbf{y}$ , respectively. The ratio between the size of the macroscopic and microscopic domains are related by a small positive size scale ratio,  $\zeta$ , (i.e.,  $0 < \zeta \ll 1$ ), and  $\mathbf{y} = \mathbf{x}/\zeta$ . Employing the method of multiple scales [5], an arbitrary response field,  $f^{\zeta}(\mathbf{x})$ , is

expressed in terms of the micro- and macroscopic coordinates:

$$f^\zeta(\mathbf{x}) = f(\mathbf{x}, \mathbf{y}(\mathbf{x})) \quad (8)$$

Utilizing the chain rule:

$$f_{,i}^\zeta(\mathbf{x}) = f_{,x_i}(\mathbf{x}, \mathbf{y}) + \frac{1}{\zeta} f_{,y_i}(\mathbf{x}, \mathbf{y}) \quad (9)$$

The response fields are assumed to be locally periodic over the domain of the microstructure throughout the deformation process:

$$f(\mathbf{x}, \mathbf{y}) = f(\mathbf{x}, \mathbf{y} + \mathbf{k}\hat{\mathbf{y}}) \quad (10)$$

in which,  $\hat{\mathbf{y}}$  represents the period of the microstructure and  $\mathbf{k}$  is a  $n_{\text{sd}} \times n_{\text{sd}}$  diagonal matrix consisting of integer entries.

### 3 Reduced order computational homogenization with eigenstrains

The proposed methodology for multiscale modeling employs the asymptotic homogenization with multiple spatial scales. In this context, the displacement field of the heterogeneous material is decomposed using a two-scale asymptotic expansion:

$$u_i(\mathbf{x}, \mathbf{y}, t) = \bar{u}_i(\mathbf{x}, t) + \zeta u_i^1(\mathbf{x}, \mathbf{y}, t) \quad (11)$$

in which,  $\bar{\mathbf{u}}$  and  $\mathbf{u}^1$  are the macroscopic and microscopic displacement fields, respectively. The  $O(1)$  displacement field is taken to be independent of the microscale coordinates and constitutes the homogenized displacement field, whereas the  $O(\zeta)$  displacement field accounts for the microstructural perturbations due to the microstructural heterogeneity. The two-scale decomposition of the displacement field is substituted into the original governing equations (i.e., Eqs. 2-7), and asymptotic analysis is performed, which results in coupled macro- and microscale problems. In order to reduce the computational complexity associated with solving the microscale boundary value problem, the eigendeformation-based reduced order approach is utilized. In the context of damage mechanics, detailed descriptions of the asymptotic analysis and the model order reduction are provided in Ref. [40]. In what follows, we summarize the resulting macro- and the microscale equations that form the basis of the reduced order model developed in this manuscript.

### 3.1 Macroscale problem

Asymptotic expansion of the response fields, the consequent asymptotic analysis with multiple spatial scales, and homogenization of the resulting equilibrium equations result in the homogenized macroscale equilibrium equation defined over the macroscopic domain,  $\Omega$ :

$$\bar{\sigma}_{ij,x_j}(\mathbf{x}, t) + \bar{b}_i(\mathbf{x}, t) = 0; \quad \mathbf{x} \in \Omega \quad (12)$$

in which,  $\bar{\boldsymbol{\sigma}}$  and  $\bar{\mathbf{b}}$  denote the macroscopic stress tensor and the body force, respectively. The macroscopic stress and body force terms are obtained through volume-averaging (homogenization) of the respective fields over the domain of the microstructure,  $\Theta$ :

$$\bar{f}(\mathbf{x}, t) := \langle f(\mathbf{x}, \mathbf{y}, t) \rangle_{\Theta} = \frac{1}{|\Theta|} \int_{\Theta} f d\mathbf{y} \quad (13)$$

where,  $|\Theta|$  is the volume of the microstructure domain. The stress field is expressed as a function of the microscale displacement field as:

$$\bar{\sigma}_{ij}(\mathbf{x}, t) = \left\langle L_{ijkl}(\mathbf{y}) \left[ \bar{\epsilon}_{kl}(\mathbf{x}, t) + u_{(k,y_l)}^1(\mathbf{x}, \mathbf{y}, t) - \mu_{kl}(\mathbf{x}, \mathbf{y}, t) \right] \right\rangle_{\Theta} \quad (14)$$

where, the macroscopic strain is obtained as the symmetric gradient of the homogenized displacement field:

$$\bar{\epsilon}_{ij}(\mathbf{x}, t) = \bar{u}_{(i,x_j)}(\mathbf{x}, t) \quad (15)$$

Assuming that the boundary data vary with respect to the macroscopic scale only, the boundary conditions of the macroscale problem are expressed as:

$$\bar{u}_i(\mathbf{x}, t) = \hat{u}_i(\mathbf{x}, t) \quad \mathbf{x} \in \partial\Omega^u \quad (16)$$

$$\bar{\sigma}_{ij}(\mathbf{x}, t) n_j = \hat{t}_i(\mathbf{x}, t) \quad \mathbf{x} \in \partial\Omega^t \quad (17)$$

The macroscopic problem does not have an explicit constitutive relationship to close the boundary value problem. Instead, the macroscopic strain and stress are linked through the microstructural deformation state by Eq. 14. The microscopic deformation state is computed numerically based on the reduced order microscopic problem defined below.

### 3.2 Reduced-order microscale problem

Asymptotic analysis of the original governing system of equations also results in the microscale equilibrium equation defined over the domain of the microstructure as:

$$\left\{ L_{ijkl}(\mathbf{y}) \left[ \bar{\epsilon}_{kl}(\mathbf{x}, t) + u_{(k,y_l)}^1(\mathbf{x}, \mathbf{y}, t) - \mu_{kl}(\mathbf{x}, \mathbf{y}, t) \right] \right\}_{,y_j} = 0; \quad \mathbf{y} \in \Theta \quad (18)$$

where, the macroscopic strain acts as the loading function for the microscale problem.

The local periodicity of the microstructure response fields defined in Eq. 10 naturally leads to periodic boundary conditions for the microscale problem. For a rectangular (or cuboidal) shaped RVE domain, the boundary is split into  $n_{\text{sd}}$  pairs of parallel sides (or faces) denoted by  $\partial\Theta_\xi$ . The periodic boundary conditions are then expressed as:

$$u_i^1(\mathbf{x}, \mathbf{y}, t) = u_i^1(\mathbf{x}, \mathbf{y} - l_\xi \mathbf{n}_\xi, t); \quad \mathbf{y} \in \partial\Theta_\xi; \quad \xi = 1, \dots, n_{\text{sd}} \quad (19)$$

in which,  $\mathbf{n}_\xi$  is the unit outward normal on  $\partial\Theta_\xi$ , and  $l_\xi$  is the length of the microstructure domain along  $\mathbf{n}_\xi$ . In order to restrict rigid body motion, displacement is constrained at the microstructure domain vertices. Equation 18 along with the damage evolution equations (described below) and the periodic boundary conditions constitute the microscale boundary value problem.

Eigendeformation-based reduced order homogenization is based on expressing the microscale displacement field in terms of microstructural influence functions as [40]:

$$u_i^1(\mathbf{x}, \mathbf{y}, t) = H_{ikl}(\mathbf{y}) \bar{\epsilon}_{kl}(\mathbf{x}, t) + (h_{ikl} * \mu_{kl})(\mathbf{x}, \mathbf{y}, t) \quad (20)$$

where,  $\mathbf{H}$  and  $\mathbf{h}$  are respectively the elastic and damage-induced influence functions; and  $*$  denotes convolution performed over the microstructure domain,  $\Theta$ . In the absence of damage or other inelastic effects, the linearity of the microscale displacement field with respect to the macroscopic strains is exploited (i.e., the first term on the right hand side of Eq. 20). The microscale problem then results in the influence function problem of the classical linear-elastic mathematical homogenization theory [5]. The second component is obtained based on the Green's function approach, in which the inelastic strain field is viewed as the spatially variable "force" acting on the microstructure [13].

Consider the following reduced basis representation of the inelastic strain,  $\boldsymbol{\mu}^{(\alpha)}$  and damage,  $\omega^{(\alpha)}$  fields, respectively:

$$\mu_{ij}(\mathbf{x}, \mathbf{y}, t) = \sum_{\alpha=1}^n N^{(\alpha)}(\mathbf{y}) \mu_{ij}^{(\alpha)}(\mathbf{x}, t) \quad (21)$$

$$\omega(\mathbf{x}, \mathbf{y}, t) = \sum_{\alpha=1}^n N^{(\alpha)}(\mathbf{y}) \omega^{(\alpha)}(\mathbf{x}, t) \quad (22)$$

where,  $N^{(\alpha)}$  denotes a mesomechanical shape function;  $n$  the order of the reduced basis; and  $\boldsymbol{\mu}^{(\alpha)}$  and  $\omega^{(\alpha)}$  are the mesomechanical inelastic strain coefficients and phase damage coeffi-

cients, respectively. The mesomechanical coefficients have the following nonlocal forms:

$$\mu_{ij}^{(\alpha)}(\mathbf{x}, t) = \int_{\Theta} \varphi^{(\alpha)}(\mathbf{y}) \mu_{ij}(\mathbf{x}, \mathbf{y}, t) d\mathbf{y} \quad (23)$$

$$\omega^{(\alpha)}(\mathbf{x}, t) = \int_{\Theta} \varphi^{(\alpha)}(\mathbf{y}) \omega(\mathbf{x}, \mathbf{y}, t) d\mathbf{y} \quad (24)$$

in which,  $\varphi^{(\alpha)}$  are mesomechanical weight functions.

The reduced order representation of the inelastic response fields are therefore characterized by the model order parameter,  $n$ , the mesomechanical shape functions and the weight functions. Naturally,  $n$  is chosen low enough to ensure that the size of the resulting reduced system of equations to evaluate the microscale displacement field is small. The mesomechanical shape functions differ from the standard finite element shape functions in the sense that they are coarser and require only  $C^{-1}$  continuity (since they are defined over strain fields). Equations 21-24 are consistent and imply orthonormality between the shape and weight functions:

$$\int_{\Theta} \varphi^{(\alpha)}(\mathbf{y}) N^{(\beta)}(\mathbf{y}) d\mathbf{y} = \delta_{\alpha\beta} \quad (25)$$

in which  $\delta_{\alpha\beta}$  is the Kronecker delta.

Taking the symmetric gradient of the microscale displacement field in Eq. 20 and employing Eq. 3 yields:

$$\mu_{ij}(\mathbf{x}, \mathbf{y}, t) = \omega(\mathbf{x}, \mathbf{y}, t) [A_{ijkl}(\mathbf{y}) \bar{\epsilon}_{kl}(\mathbf{x}, t) + (g_{ijkl} * \mu_{kl})(\mathbf{x}, \mathbf{y}, t)] \quad (26)$$

where,  $\mathbf{A} = \mathbf{I} + \mathbf{G}$  with  $G_{ijkl} = H_{(i,y_j)kl}$  and  $g_{ijkl} = h_{(i,y_j)kl}$ , and  $\mathbf{I}$  is the fourth order identity tensor. Premultiplying both sides of Eq. 26 by the weight function,  $\varphi^{(\beta)}$ , integrating over the microstructure domain and substituting the reduced basis decompositions (i.e., Eqs. 21-24) yield ( $\beta = 1, \dots, n$ ):

$$\begin{aligned} \Phi^{(\beta)} := \sum_{\gamma=1}^n \left[ I_{ijkl} \delta_{\beta\gamma} - \sum_{\alpha=1}^n \omega^{(\alpha)}(\mathbf{x}, t) \tilde{P}_{ijkl}^{(\alpha\beta\gamma)} \right] \mu_{kl}^{(\gamma)}(\mathbf{x}, t) \\ - \sum_{\alpha=1}^n \omega^{(\alpha)}(\mathbf{x}, t) \tilde{A}_{ijkl}^{(\alpha\beta)} \bar{\epsilon}_{kl}(\mathbf{x}, t) = 0 \end{aligned} \quad (27)$$

in which, the coefficient tensors,  $\tilde{\mathbf{P}}^{(\alpha\beta\gamma)}$  and  $\tilde{\mathbf{A}}^{(\alpha\beta)}$  are expressed in terms of the influence, shape and weight functions as:

$$\tilde{P}_{ijkl}^{(\alpha\beta\gamma)} = \int_{\Theta} \varphi^{(\beta)}(\mathbf{y}) N^{(\alpha)}(\mathbf{y}) P_{ijkl}^{(\gamma)}(\mathbf{y}) d\mathbf{y} \quad (28)$$

$$\tilde{A}_{ijkl}^{(\alpha\beta)} = \int_{\Theta} \varphi^{(\beta)}(\mathbf{y}) N^{(\alpha)}(\mathbf{y}) A_{ijkl}(\mathbf{y}) d\mathbf{y} \quad (29)$$

and,  $\mathbf{P}^{(\gamma)}(\mathbf{y}) = (\mathbf{g} * N^{(\gamma)})(\mathbf{y})$ .

The reduced order microscale problem then reduces to the simultaneous evaluation of the nonlinear system of equations  $\Phi^{(\beta)} = 0$  ( $\beta = 1, \dots, n$ ) along with the appropriate damage evolution equations. By virtue of the elastic and inelastic influence functions, the microstructural equilibrium is automatically ensured for damage and inelastic strain fields that satisfy Eq. 27.

The macroscopic stress is expressed as a function of the inelastic strain coefficients by substituting the microscale displacement decomposition (Eq. 18) into Eq. 14, and exploiting the reduced basis decomposition of the inelastic fields:

$$\bar{\sigma}_{ij}(\mathbf{x}, t) = \bar{L}_{ijkl} \bar{\epsilon}_{kl}(\mathbf{x}, t) + \sum_{\alpha=1}^n M_{ijkl}^{(\alpha)} \mu_{kl}^{(\alpha)}(\mathbf{x}, t) \quad (30)$$

where, the stiffness tensors,  $\bar{\mathbf{L}}$  and  $\bar{\mathbf{M}}^\alpha$  are expressed as:

$$\bar{L}_{ijkl} = \langle L_{ijmn}(\mathbf{y}) A_{mnkl}(\mathbf{y}) \rangle \quad (31)$$

$$M_{ijkl}^{(\alpha)} = \left\langle L_{ijmn}(\mathbf{y}) \left[ P_{mnkl}^{(\alpha)}(\mathbf{y}) - I_{mnkl} N^{(\alpha)}(\mathbf{y}) \right] \right\rangle_{\Theta} \quad (32)$$

## 4 Method of overlapping failure paths

The accuracy and computational efficiency of the reduced order model is related to the model order,  $n$  as well as the selection of the shape and weight functions of the ROM. In this section, we present a new model selection strategy, which (a) allows for the reduced order model to have a non-orthogonal basis and (b) formulates a strategy for identifying the basis functions based on a-priori RVE simulations.

In order to ensure physically consistent reduced model discretization, the shape and weight functions are taken to satisfy the following three additional constraints:

$$\sum_{\alpha=1}^n N^{(\alpha)}(\mathbf{y}) = 1; \quad \mathbf{y} \in \Theta \quad (33)$$

$$\varphi^{(\alpha)}(\mathbf{y}) \geq 0; \quad \mathbf{y} \in \Theta \quad (34)$$

$$\int_{\Theta} \varphi^{(\alpha)}(\mathbf{y}) d\mathbf{y} = 1 \quad (35)$$

Equation 33 indicates the partition of unity of the inelastic response fields within the microstructure domain and ensures exact representation of the constant strain modes. The positivity of the weight function (Eq. 34) is necessary to eliminate negative damage contribution to the mesomechanical damage field,  $\omega^{(\alpha)}$  from any subdomain of the microstructure

based on Eq. 24. The weight function normalization condition (Eq. 35) ensures consistency of Eq. 26 under constant strain mode/damage state.

Let  ${}_i\Theta \subset \Theta$  denote the domain of phase  $i$  ( $1 \leq i \leq c$ ) within the microstructure domain. Naturally,  $\bigcup_{i=1}^c {}_i\Theta = \Theta$  and the intersections form null sets, i.e., the interfaces. Consider an alternative partitioning of the domain of the microstructure into  $n$  possibly overlapping subdomains, with  $\Theta^{(\alpha)}$  denoting the  $\alpha^{\text{th}}$  subdomain (or part) in the partition. A part is taken to lie within a single phase:  $\Theta^{(\alpha)} \subset {}_i\Theta$ . The intersection between two parts is denoted as  $\Theta^{(\alpha\beta)} \equiv \Theta^{(\alpha)} \cap \Theta^{(\beta)}$ . The intersections between multiple parts are defined by repetitive Greek superscripts:  $\Theta^{(\alpha\beta\nu\dots)} \equiv \Theta^{(\alpha)} \cap \Theta^{(\beta)} \cap \Theta^{(\nu)} \dots$ . Let  $S_k^{(\alpha)}$  denote the subdomain of  $\Theta^{(\alpha)}$ , which has  $k$  or more intersections:

$$S_0^{(\alpha)} = \Theta^{(\alpha)}; \quad S_1^{(\alpha)} = \bigcup_{\substack{\beta=1 \\ \beta \neq \alpha}}^n \Theta^{(\alpha\beta)}; \quad S_2^{(\alpha)} = \bigcup_{\substack{\beta=1 \\ \beta \neq \alpha}}^n \bigcup_{\substack{\nu=1 \\ \nu \neq \alpha, \beta}}^n \Theta^{(\alpha\beta\nu)}; \dots \quad (36)$$

and  $\Theta_k^{(\alpha)}$  denotes the subdomain of  $\Theta^{(\alpha)}$  that intersects precisely  $k - 1$  other parts:

$$\Theta_k^{(\alpha)} = S_{k-1}^{(\alpha)} \setminus S_k^{(\alpha)} \quad (37)$$

In view of Eq. 33, we consider the following shape function to describe the variation of the inelastic strain and damage fields within the microstructure domain:

$$N^{(\alpha)}(\mathbf{y}) = \begin{cases} \frac{1}{k} & \text{if } \mathbf{y} \in \Theta_k^{(\alpha)} \\ 0 & \text{if } \mathbf{y} \in \Theta \setminus \Theta^{(\alpha)} \end{cases} \quad (38)$$

The shape functions defined in Eq. 38 allow the possibility of overlapping subdomains and the resulting discretization forms a non-orthogonal basis. Given the shape functions defined in Eq. 38, the corresponding weight functions are determined such that the positivity and normality conditions given by Eqs. 34 and 35, respectively, are satisfied.

Consider the simple example illustrated in Fig. 1a to demonstrate the weight function identification process. The reduced order model consists of two parts with a total of three subdomains,  $\Theta_1^{(1)}$  and  $\Theta_1^{(2)}$  and the overlap subdomain,  $\Theta_2^{(12)}$ . Taking a piecewise constant form for the shape functions associated with the two parts as illustrated in Fig. 1b, considering piecewise constant variation of the weight functions, and employing the constraint equations defined in Eqs. 34 and 35 results in a unique description of the weight functions of the following form:

$$\varphi^{(\alpha)}(\mathbf{y}) = \begin{cases} \frac{1}{|\Theta_1^{(\alpha)}|} & \text{if } \mathbf{y} \in \Theta_1^{(\alpha)} \\ 0 & \text{elsewhere} \end{cases} \quad (39)$$

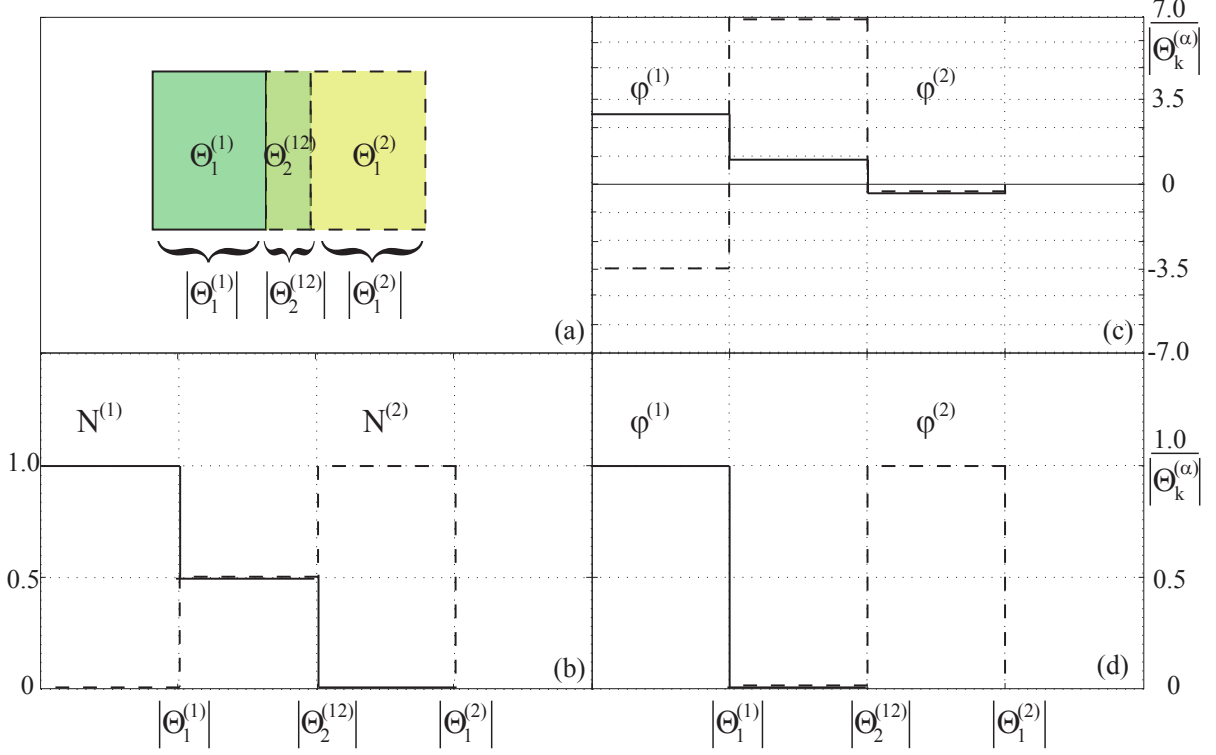


Figure 1: (a) Illustrative example of two subdomains  $\Theta_1^{(1)}$  and  $\Theta_1^{(2)}$  with the intersection denoted as  $\Theta_2^{(12)}$ ; (b) shape functions corresponding to Eq. 38; (c) Corresponding weight functions without imposing positivity constraint; (d) weight functions corresponding to imposing positivity and normality constraints.

Using the specific choices for the shape and weight functions in Eqs. 38 and 39, the coefficient tensors become:

$$\tilde{P}_{ijkl}^{(\alpha\gamma)} := \tilde{P}_{ijkl}^{(\alpha\alpha\gamma)} = \frac{1}{|\Theta_1^{(\alpha)}|} \int_{\Theta_1^{(\alpha)}} P_{ijkl}^{(\gamma)}(\mathbf{y}) d\mathbf{y} = \langle P_{ijkl}^{(\gamma)}(\mathbf{y}) \rangle_{\Theta_1^{(\alpha)}} \quad (40)$$

$$\tilde{A}_{ijkl}^{(\alpha)} := \tilde{A}_{ijkl}^{(\alpha\alpha)} = \langle A_{ijkl}(\mathbf{y}) \rangle_{\Theta_1^{(\alpha)}} \quad (41)$$

and,  $\tilde{\mathbf{P}}^{(\alpha\beta\gamma)} = \mathbf{0}$  and  $\tilde{\mathbf{A}}^{(\alpha\beta)} = \mathbf{0}$  for  $\alpha \neq \beta$ . The above coefficient tensors in the context of Eq. 27 imply that the response within the overlap region does not contribute to the computation of the damage and inelastic strain coefficients. The damage and inelastic strain fields within the overlap regions are computed as averages of the corresponding non-overlap regions. For instance, denoting the damage state within the overlap regions as  $\omega_1^{(1)}$  and  $\omega_1^{(2)}$ , respectively in the above example, the corresponding damage state within the overlap region ( $\omega^{(12)}$ ) becomes:

$$\omega^{(12)} = \frac{1}{2} \left( \omega_1^{(1)} + \omega_1^{(2)} \right) \quad (42)$$

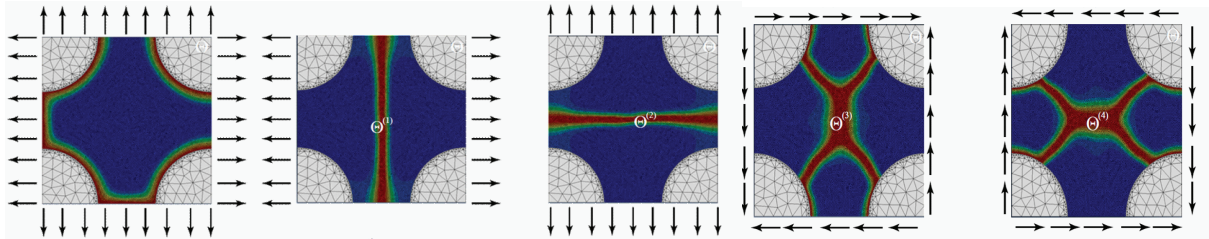


Figure 2: Schematic representation of the failure paths in a square unit cell under biaxial, uniaxial and shear loading.

using Eqs. 21 and 38. The inelastic strain field within the overlap region is obtained analogous to Eq. 42. The result that damage evolution is not tracked within the overlap region implies: (1) the size of the overlap region compared to the overall size of the parts must be small, and (2) the overlap regions must not coincide with microstructure subdomains of high stress concentration, where averaging cannot capture the damage evolution behavior.

It is easy to observe that the particular choice of the shape functions in Eq. 38 along with shape-weight function orthonormality condition (i.e., Eq.25) automatically satisfy weight function normalization condition. Relaxing the weight function positivity (Eq. 34) constraint leads to unphysical damage state. A set of piecewise constant weight functions identified for the example problem in Fig. 1a without the positivity constraint is shown in Fig. 1c. Considering the damage state described by the set of coefficients:  $\omega^{(1)} = 0$  and  $\omega^{(2)} > 0$  necessarily indicate a negative damage state within  $\Theta_1^{(1)}$ , which is not physical.

In what follows, the shape and weight functions are therefore taken to be expressed as in Eqs. 38 and Eq. 39, respectively.

## 4.1 Identification of failure paths

The efficiency and the accuracy of capturing the failure behavior in the heterogeneous material is controlled by the selection of the model order  $n$  and the way the microstructure is decomposed into parts. The premise of the current strategy in the model order selection is to track the evolution of damage within microstructure subdomains, which could form crack paths through the microstructure under prescribed loading conditions. These subdomains are denoted as “failure paths” [15].

The procedure for the identification of the failure paths is as follows with reference to the schematic illustration in Fig. 2: The failure in a microstructure subjected to a prescribed set of loading conditions admissible by the homogenization theory is simulated using direct numerical simulation until complete failure. The failure within the microstructure is tracked using nonlocal continuum damage mechanics (model described below), which identifies the path of damage as a set of equal measure in  $\mathbb{R}^{n_{sd}}$  (e.g., a volume in 3-d). The path of damage for each loading condition (i.e., failure path) is chosen as a reduced order model part. Failure

paths under different loading conditions can overlap, which is allowed in the ROM formulation described above. The remainder of the microstructure domain, which does not lie within any of the failure paths is assigned a separate part. In the square unit cell example shown in Fig. 2, biaxial, uniaxial, and pure shear conditions are used to construct the failure paths.

## 5 Alleviating post-failure spurious residual stiffness

The microscale reduced order model along with the damage evolution equations defining the failure behavior of constituent materials constitute a full nonlinear system to evaluate the microstructural behavior. When low order models are employed, this approach was shown to demonstrate a significant post-failure residual stiffness [40, 23]. The post failure residual stiffness refers to the ability of the microstructural domain to retain load carrying capacity after failure. The residual stiffness is spurious and must be alleviated to ensure accurate load redistribution at the macroscale in a failure propagation scenario. This issue has been tied to the concept of the incompatibility of the eigenstrains proposed by Mura and Furuhashi [25] as discussed in Fish et al. [23].

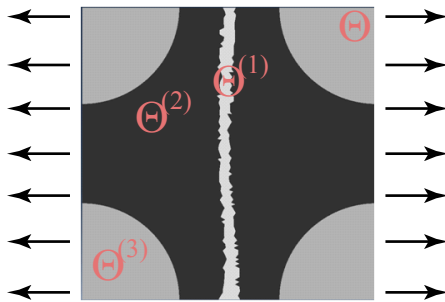


Figure 3: New set of coefficient tensors are generated based on the combination of activated failure paths, (i.e. compatible eigenstrains). The dark grey (matrix) and the light grey (fiber) regions retain their original material properties. The white region is the failure path.

In order to demonstrate this issue, we follow a simple example similar to the discussion in Ref. [23], but consider failure paths within the reduced order model. Figure 3 shows the three-part, non-overlapping reduced order model to describe the behavior of a square unit cell. A single failure path (i.e.,  $\Theta^{(1)}$ ) is considered in the model, and microstructure domain is subjected to unidirectional loading perpendicular to the failure path. Consider the onset of full damage on the failure path with no significant damage on the other parts (i.e.,  $\omega^{(1)}=1$ ;  $\omega^{(2)}=\omega^{(3)}=0$ ). Applying the damage state to Eq. 27 yields (for  $\beta = 1$ ):

$$\left( I_{ijkl} - \tilde{P}_{ijkl}^{(11)} \right) \mu_{kl}^{(1)}(\mathbf{x}, t) - \tilde{P}_{ijkl}^{(12)} \mu_{kl}^{(2)}(\mathbf{x}, t) - \tilde{P}_{ijkl}^{(13)} \mu_{kl}^{(3)}(\mathbf{x}, t) = \tilde{A}_{ijkl}^{(1)} \bar{\epsilon}_{kl}(\mathbf{x}, t) \quad (43)$$

Considering Eq. 27 for  $\beta = 2, 3$ , it is trivial to see that  $\boldsymbol{\mu}^{(2)} = \boldsymbol{\mu}^{(3)} = \mathbf{0}$ , which leads to:

$$\mu_{ij}^{(1)}(\mathbf{x}, t) = \left( I - \tilde{P}^{(11)} \right)_{ijmn}^{-1} \tilde{A}_{mnkl}^{(1)} \bar{\epsilon}_{kl}(\mathbf{x}, t) \equiv Q_{ijkl} \bar{\epsilon}_{kl}(\mathbf{x}, t) \quad (44)$$

Using the reduced order shape functions defined in Eq. 38 along with Eq. 31, and considering a piecewise-constant tensor of elastic moduli within the microstructure:

$$M_{ijkl}^{(1)} = c_1 L_{ijmn}^{(1)} \left( \tilde{P}_{mnkl}^{(11)} - I_{mnkl} \right) + \sum_{\alpha=2}^3 c_\alpha L_{ijmn}^{(\alpha)} \tilde{P}_{mnkl}^{(\alpha 1)} \quad (45)$$

where,  $c_\alpha$  denotes the volume fraction of part,  $\alpha$  (i.e.,  $c_\alpha = |\Theta^{(\alpha)}|/|\Theta|$ ); and  $\mathbf{L}^{(\alpha)}$  is the tensor of elastic moduli of the constituent that occupies the domain of part  $\alpha$ . Expressing the homogenized tensor of elastic moduli in terms of the part average polarization tensors,  $\tilde{\mathbf{A}}^{(\alpha)}$ :

$$\bar{L}_{ijkl} = \sum_{\alpha=1}^3 c_\alpha L_{ijmn}^{(\alpha)} \tilde{A}_{mnkl}^{(\alpha)} \quad (46)$$

Substituting Eqs. 44-46 into the macroscopic stress expression (Eq. 30) yields:

$$\bar{\sigma}_{ij}(\mathbf{x}, t) = \sum_{\alpha=2}^3 c_\alpha L_{ijpq}^{(\alpha)} \left( \tilde{A}_{pqkl}^{(\alpha)} + \tilde{P}_{pqmn}^{(\alpha 1)} Q_{mnkl} \right) \bar{\epsilon}_{kl}(\mathbf{x}, t) \quad (47)$$

The expression above is generally non-zero [23, 25]. Fish et al. [23] employed the idea of compatible eigenstrains such that the macroscopic stress vanishes, which amounts to introducing a new set of coefficient tensors  $\hat{\mathbf{P}}^{(\alpha 1)}$  to replace  $\tilde{\mathbf{P}}^{(\alpha 1)}$  in Eq. 47 upon detection of full damage within part 1, such that:

$$\hat{P}_{ijkl}^{(\alpha 1)} = -\tilde{A}_{ijmn}^{(\alpha)} Q_{mnkl}^{-1} \quad (48)$$

which effectively enforces the loss of load carrying capacity (i.e., zero stiffness). One drawback of this approach is that the loss of load carrying capacity is enforced at all loading directions. In the context of the failure path illustrated in Fig. 3, the microstructure must retain stiffness in the directions transverse to the failure path even after full damage within the failure path. (e.g.,  $\bar{\sigma}_{11} = 0$ , but  $\bar{\sigma}_{22}, \bar{\sigma}_{12} \neq 0$ ).

A simple alternative approach is proposed to alleviate the spurious residual stresses displayed in ROMs only along directions of failure. Let  $\varsigma$  denote the set of coefficient tensors of the reduced order model:

$$\varsigma := \left\{ \tilde{\mathbf{A}}^{(\alpha)}, \mathbf{M}^{(\alpha)}, \tilde{\mathbf{P}}^{(\alpha\beta)}; \mathbf{L}^{(\alpha)} \mid \alpha, \beta = 1, 2, \dots, n \right\} \quad (49)$$

in which the coefficient tensors are written in vector notation (bold symbols) for simplicity.  $\varsigma$  is used for as long as  $\omega^{(\alpha)} < 1, \forall \alpha$ , which is prior to the onset of full damage in a failure path. We define a new set of coefficient tensors such that:

$$\varsigma_1^{\alpha_1} := \left\{ \hat{\mathbf{A}}^{(\alpha)}, \hat{\mathbf{M}}^{(\alpha)}, \hat{\mathbf{P}}^{(\alpha\beta)}; \mathbf{L}^{(\alpha \neq \alpha_1)}, \hat{\mathbf{L}}^{(\alpha_1)} = \iota \mathbf{L}^{(\alpha_1)} \right. \\ \left. \left| \alpha, \beta = 1, 2, \dots, n; \alpha_1 \in \{1, 2, \dots, n\}; 0 < \iota < 1 \right\} \quad (50)$$

$\varsigma_1^{\alpha_1}$  is computed with a tensor of elastic moduli in part  $\alpha_1$  degraded by factor  $\iota$ . The idea is to employ  $\varsigma_1^{\alpha_1}$  in the reduced order model to replace  $\varsigma$ , when failure is detected in path  $\alpha_1$  (i.e.,  $\omega^{(\alpha \neq \alpha_1)} < 1, \omega^{(\alpha_1)} \simeq 1$ ). For each failure path,  $\varsigma_1^\alpha$  is computed at the preprocessing stage along with  $\varsigma$ , prior to the macroscale analysis. The coefficient tensors with degraded properties in the failure path approximates the presence of a through crack across the microstructure domain, eliminating the stiffness properties along the appropriate loading directions.

This idea can be generalized to account for secondary failures that occur within a microstructure upon a change in loading direction. For instance, considering a new set of coefficient tensors defined as:

$$\varsigma_2^{\alpha_1, \alpha_2} := \left\{ \hat{\mathbf{A}}^{(\alpha)}, \hat{\mathbf{M}}^{(\alpha)}, \hat{\mathbf{P}}^{(\alpha\beta)}; \mathbf{L}^{(\alpha \neq \alpha_1, \alpha_2)}, \hat{\mathbf{L}}^{(\alpha_1)} = \iota \mathbf{L}^{(\alpha_1)}, \hat{\mathbf{L}}^{(\alpha_2)} = \iota \mathbf{L}^{(\alpha_2)} \right. \\ \left. \left| \alpha, \beta = 1, 2, \dots, n; \alpha_1 \in \{1, 2, \dots, n\}, \alpha_2 \in \{1, 2, \dots, n\}; 0 < \iota \ll 1 \right\} \quad (51)$$

$\varsigma_2^{\alpha_1, \alpha_2}$  is employed when two cascading failures are detected ( $\omega^{(\alpha \neq \alpha_1)} < 1, \omega^{(\alpha_1)} \simeq 1, \omega^{(\alpha_2)} \simeq 1$ ) in parts  $\alpha_1$  and  $\alpha_2$  by replacing  $\varsigma_1^{\alpha_1}$  with  $\varsigma_2^{\alpha_1, \alpha_2}$  upon detection of the second failure (note that  $\varsigma_2^{\alpha_1, \alpha_2} = \varsigma_2^{\alpha_2, \alpha_1}$ ). In the current manuscript, only the ‘‘first-order’’ approach has been computationally implemented and verified.

The proposed method to alleviate post-failure residual stiffness requires computation and storage of  $n$  additional sets of coefficient tensors compared to the standard EHM, which are computed off-line, prior to the macroscale analysis. There is insignificant additional computational cost of evaluating the nonlinear macroscale problem using the proposed approach.

## 6 Numerical verification

Numerical verification experiments were conducted to assess the capabilities of the proposed reduced order modeling approach compared to the finite element simulations in which the material microstructure is fully resolved. The numerical experiments were conducted by considering two particulate composite microstructures with geometry and discretization as shown in Fig. 4. The first microstructure is a cubic unit cell, whereas the second microstructure consists of randomly positioned particles with varying sizes embedded in the matrix. The particle

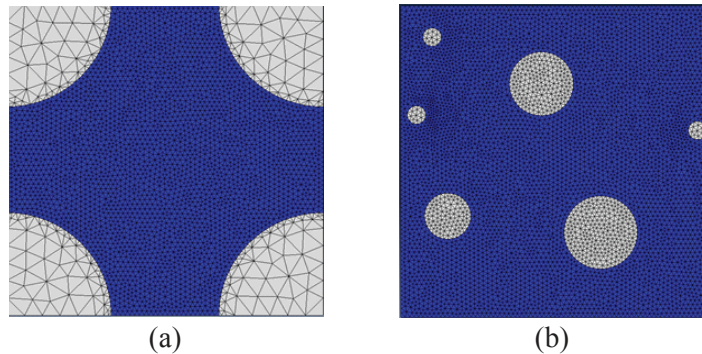


Figure 4: Unit (a) cubic- and (b) random microscopic cell geometry and discretization.

volume fractions for the two microstructures are 34% and 11% for cubic and random cells, respectively. The characteristic length of the matrix material is taken to be  $1/8$  of the size of the RVE for both microstructures. The elastic modulus and the Poisson's ratio for the fiber are  $E^{(f)} = 400$  GPa and  $\nu^{(f)} = 0.15$ ; for the matrix they are  $E^{(m)} = 115$  GPa and  $\nu^{(m)} = 0.3$ . The fiber is taken to be linear elastic and the matrix is modeled using continuum damage model described below.

The verification study discussed in this section consists of (1) the description of the continuum damage mechanics model used to idealize the progressive damage evolution within the matrix material; (2) the selection of the reduced order models for the random and cubic cells based on the method of failure paths; and (3) assessment of performance of the reduced order models compared to the direct finite element method. The effects of overlapping vs. non-overlapping paths as well as the inclusion of compatible eigenstrains are also demonstrated.

## 6.1 Damage evolution model

The failure behavior within the matrix phase is idealized using a nonlocal continuum damage mechanics model of integral type [43]. The finite element simulations in the verification study as well as in the identification of the ROM use the nonlocal damage model described below. Damage evolution within each failure path in the context of the ROM uses the same form for the damage evolution equations but do not consider the nonlocal component since each failure path is already characterized by the characteristic length within the microstructure through the failure paths. Hence, the reduced order model is microscopically nonlocal.

Damage is taken to follow a characteristic function,  $\Phi$ , such that:

$$\omega(\mathbf{y}, t) = \Phi(\kappa(\mathbf{y}, t)); \quad \frac{\partial \Phi(\kappa)}{\partial \kappa} \geq 0 \quad (52)$$

where,  $\Phi$  is taken to be of an arctangent form [22]:

$$\Phi = \frac{\text{atan}(a\kappa(\mathbf{y}, t) - b) + \text{atan}(b)}{\pi/2 + \text{atan}(b)} \quad (53)$$

in which,  $a$  and  $b$  are material parameters.  $\kappa$  is a history variable that provides the maximum value of the nonlocal equivalent strain,  $v_{nl}$ , throughout the loading history:

$$\kappa(\mathbf{y}, t) = \max \{v_{nl}(\mathbf{y}, \tau) | \tau \leq t\} \quad (54)$$

The nonlocal damage equivalent strain is expressed using the nonlocal integral in terms of the local equivalent strain,  $v$ , as:

$$v_{nl}(\mathbf{y}, t) = \frac{\int_{\Theta} \lambda(\mathbf{y} - \hat{\mathbf{y}}) v(\hat{\mathbf{y}}, t) d\hat{\mathbf{y}}}{\int_{\Theta} \lambda(\hat{\mathbf{y}}) d\hat{\mathbf{y}}} \quad (55)$$

The nonlocal weighting of the damage equivalent strain,  $\lambda$ , is expressed using the Wendland Radial Basis Function [50]:

$$\lambda(\hat{\mathbf{y}}) = \begin{cases} \left(1 - \frac{\|\hat{\mathbf{y}}\|}{l_c}\right)^4 \left(4\frac{\|\hat{\mathbf{y}}\|}{l_c} + 1\right) & \|\hat{\mathbf{y}}\| \leq l_c \\ 0 & \|\hat{\mathbf{y}}\| > l_c \end{cases} \quad (56)$$

in which,  $l_c$  denotes the characteristic length defining the span of the radial basis.

The local damage equivalent strain,  $v$ , is the metric that drives the accumulation of damage. A form similar to Mazars' model [33] is employed in this study:

$$v = \sqrt{\sum_{i=1}^{n_{sd}} \langle v_i \rangle_+^2} \quad (57)$$

where,  $\langle \cdot \rangle_+$  denotes the Macaulay brackets.  $v_i$  are computed using the modified Hamilton's theorem (e.g., in 3-d):

$$v_i^3 - I_1 v_i^2 + I_2 v_i - I_3 = 0 \quad (58)$$

in which,  $I_1$ ,  $I_2$  and  $I_3$  are:

$$I_1 = (\epsilon_{11} + \epsilon_{22} + \epsilon_{33}) \quad (59)$$

$$I_2 = (\epsilon_{11}\epsilon_{22} + \epsilon_{22}\epsilon_{33} + \epsilon_{33}\epsilon_{11} - k(\epsilon_{12}^2 + \epsilon_{23}^2 + \epsilon_{13}^2)) \quad (60)$$

$$I_3 = (\epsilon_{11}\epsilon_{22}\epsilon_{33} - k(\epsilon_{11}\epsilon_{23}^2 + \epsilon_{22}\epsilon_{13}^2 + \epsilon_{33}\epsilon_{12}^2 - 2\epsilon_{12}\epsilon_{13}\epsilon_{23})) \quad (61)$$

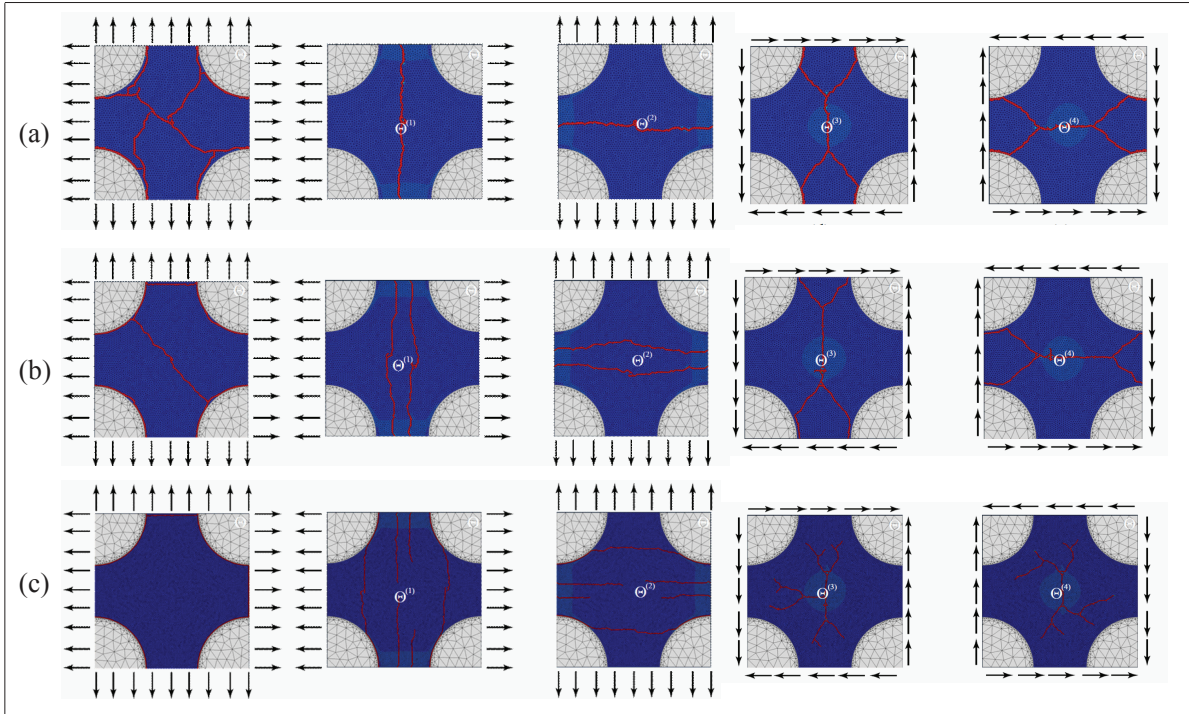


Figure 5: Symmetric microstructure with local model (a) coarse mesh: 6,698 elements; (b) medium mesh: 11,242 elements; (c) fine mesh: 24,848 elements.

with  $k$  an anisotropy parameter. Setting  $k = 1$  implies  $I_2$  and  $I_3$  are the second and third strain invariants, respectively and  $v_i$  are the principal stresses, recovering Mazars' law. The fitting parameter,  $k \neq 1$  introduces anisotropy in failure with respect to shear and normal stress components.

## 6.2 Characterization of the reduced order models

Microstructural scale simulations were performed to construct the reduced order models for the microstructures. First, we demonstrate the need to perform nonlocal failure modeling to capture reasonable failure paths to be employed in the reduced order model development. Microstructure simulations were performed with local and nonlocal damage models to illustrate this point. Mesh dependency of local damage models are very well understood in the literature [43, 3, 29]. Our objective is to demonstrate that the local damage consideration not only affects the post-peak stress-strain behavior, but also the paths of failure, which complicates the reduced model development. Failure regions in the cubic cell under uniaxial and shear loadings using local and nonlocal damage models are shown in Figs. 5 and 6, respectively. Simulations using coarse (Fig. 5a), medium (Fig. 5b), and fine (Fig. 5c) discretizations are performed. The three discretizations consist of 6,698, 11,242 and 24,848 elements respectively. The ratio of

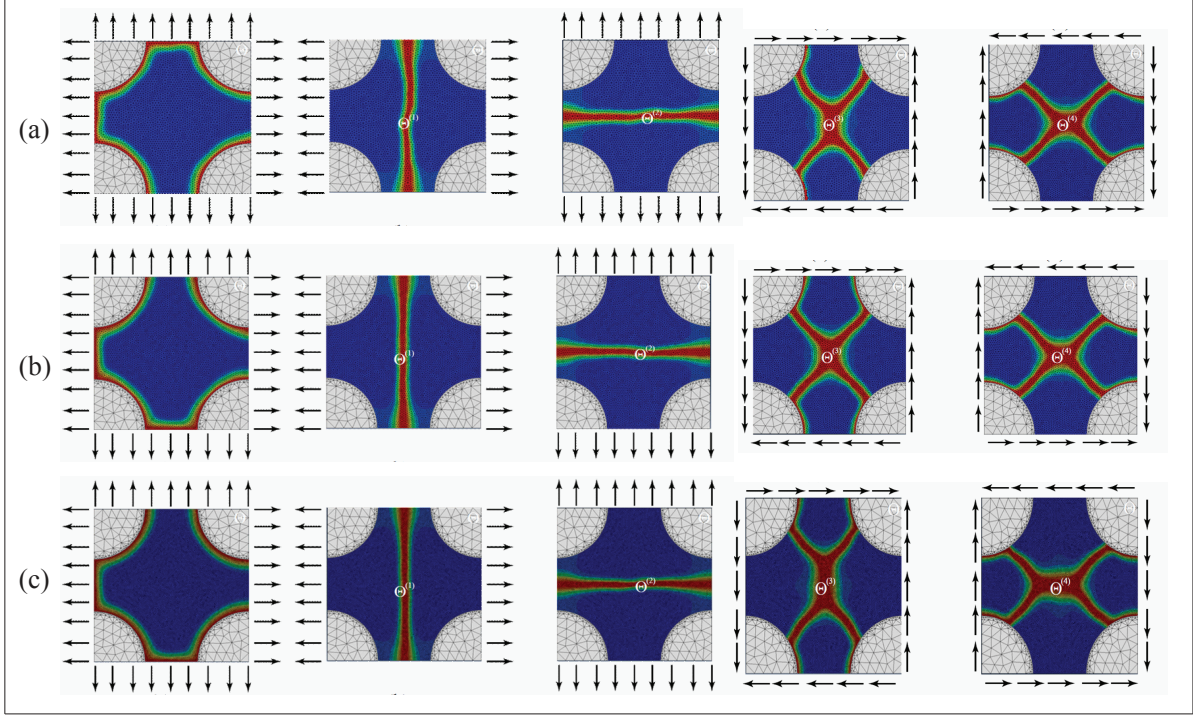


Figure 6: Symmetric microstructure with nonlocal model (a) coarse mesh: 6,698 elements; (b) medium mesh: 11,242 elements; (c) fine mesh: 24,848 elements.

the characteristic length to the cell size is set to  $1/8$  in the nonlocal simulations. Simulations performed using the local model (Fig. 5) clearly demonstrate that the failure strains localize in single element wide regions. In addition, as the mesh is refined, the failure does not converge to a single path, instead multiple failure paths are observed in highly dense meshes. Figure 6 shows the effect of employing the nonlocal damage model. As the mesh is refined, the failure paths remain unchanged and the mesh dependency is not observed. The load-displacement curves for all the nonlocal mesh refinements also exhibit nearly identical peak load. While the mesh convergence analysis is demonstrated on the square cell, the behavior and the outcome is similar for the random cell. The study on the random cell is omitted for brevity.

The failure paths and the reduced models for the cubic and random cells are therefore built based on the outcome of the nonlocal microstructural analyses. For each microstructure simulation, the failure path is identified as the set of elements for which the damage value,  $\omega \geq \omega_{cr} = 0.99$ . At this state, complete loss of load carrying capacity is observed at the scale of the cell. The failure paths were identified using the nonlocal simulation with the coarse mesh for the cubic cell as shown in Fig. 7, since the failure paths remain virtually unchanged under further refinement. The square cell matrix and reinforcements are discretized using 6,240 and 458 elements, respectively. The mesh employed for the random cell consisted of

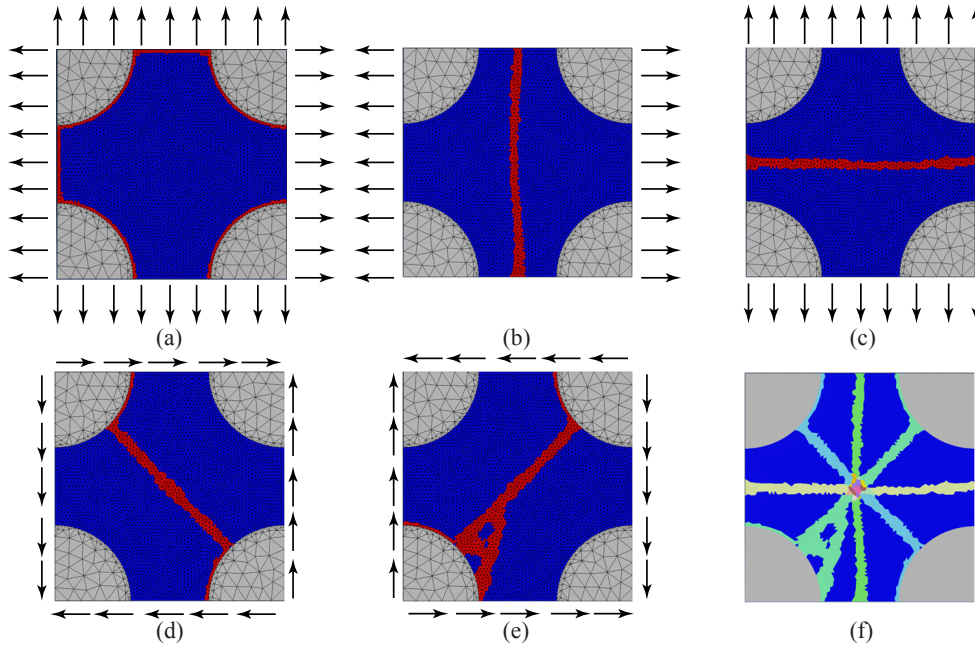


Figure 7: The partitioning and model reduction strategy. Cubic cell profiles are shown when subjected to (a) uniform biaxial loading; (b) uniaxial in the lateral direction; (c) uniaxial in the vertical direction; (d) shear loading along the positive direction; (e) shear loading along the negative direction; (f) overlapping failure partition.

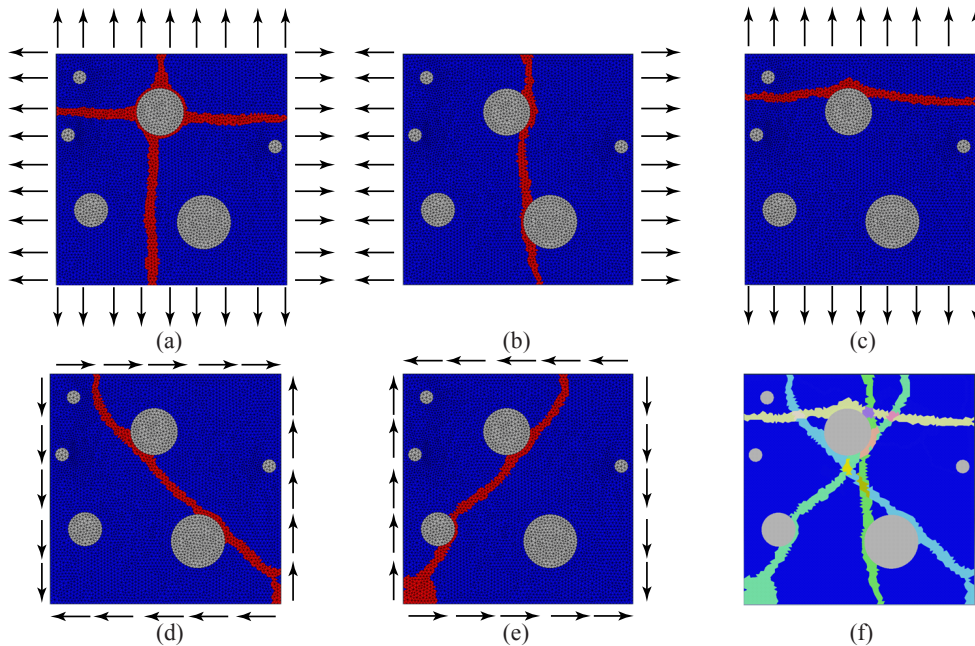


Figure 8: The partitioning and model reduction strategy. Random cell profiles are shown when subjected to (a) uniform biaxial loading; (b) uniaxial in the lateral direction; (c) uniaxial in the vertical direction; (d) shear loading along the positive direction; (e) shear loading along the negative direction; (f) overlapping failure partition.

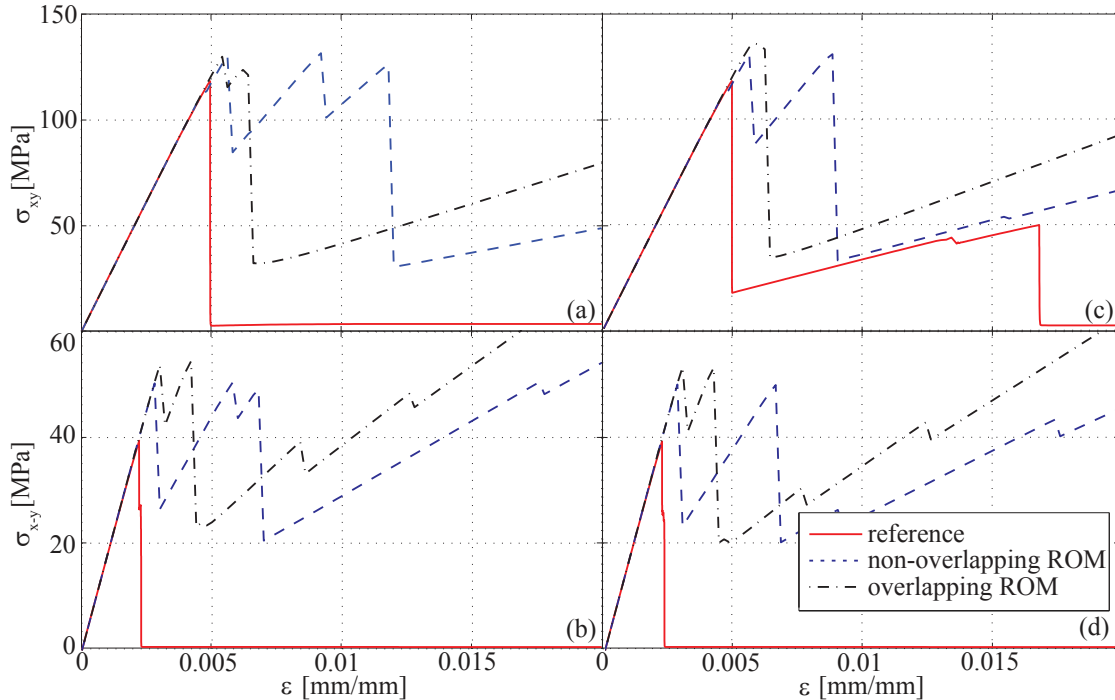


Figure 9: Stress-strain curves when subjected to (a) positive shear loading; (b) negative shear loading; (c) uniaxial in the lateral direction; (d) uniaxial in the vertical direction.

11,241 elements. The random cell matrix and reinforcements are discretized using 10,072 and 1,169 elements.

For each microstructure, we create two reduced order models: overlapping and non-overlapping. Both models are built based on failure paths generated under biaxial, two unidirectional and two shear loading as illustrated in Figs. 7 and 8. For non-overlapping models, the failure paths are separated into multiple parts and intersecting parts of the paths are considered as separate parts themselves. For cubic cells, the order of overlapping and non-overlapping models are  $n = 6$  and  $n = 15$ , respectively. For random cells the ROM with overlapping parts has the order  $n = 6$ , whereas the ROM with non-overlapping parts has  $n = 12$ . Both models also consider the remainder of the matrix phase (which lay outside any of the failure paths) to be a separate part of the ROM. Significant damage or failure is not anticipated to occur in this part. It is therefore clear that the overlapping failure path approach provide a significant computational advantage compared to the non-overlapping method.

### 6.3 Microstructure analysis

The performance of the reduced order models are assessed when the microstructures are subjected to the loading conditions shown in Figs. 7 and 8. Figure 9 illustrates the comparison between the macroscale stress-strain curves of the cubic cell as computed by the direct finite

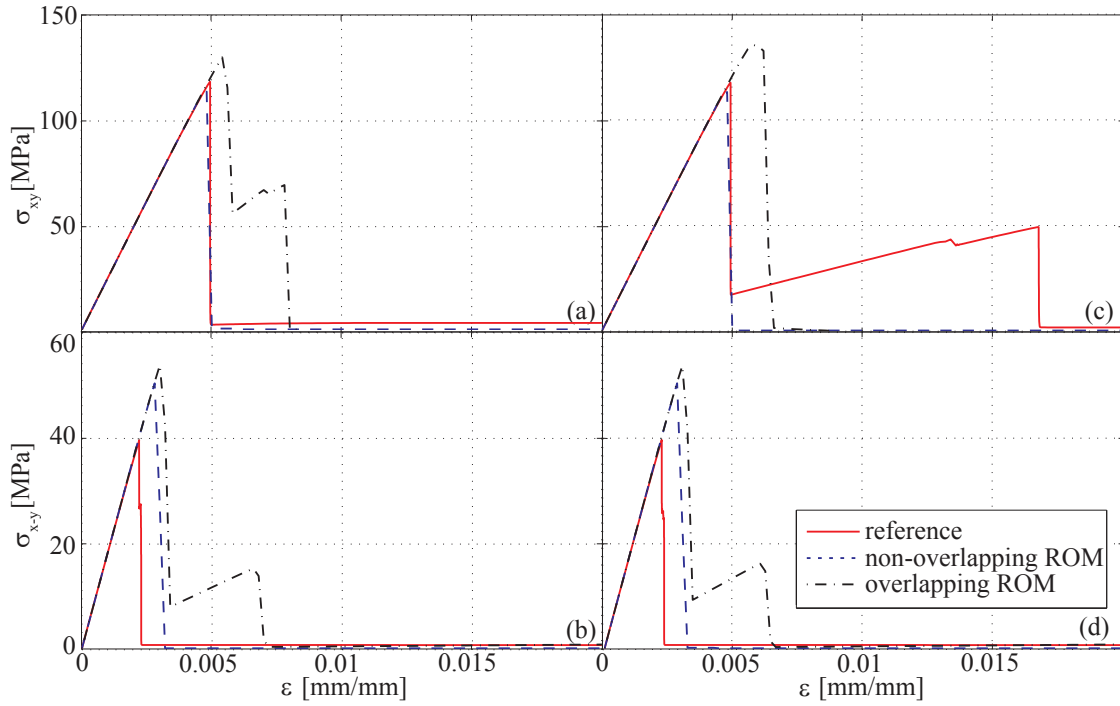


Figure 10: Stress-strain curves when subjected to (a) positive shear loading; (b) negative shear loading; (c) uniaxial in the lateral direction; (d) uniaxial in the vertical direction.

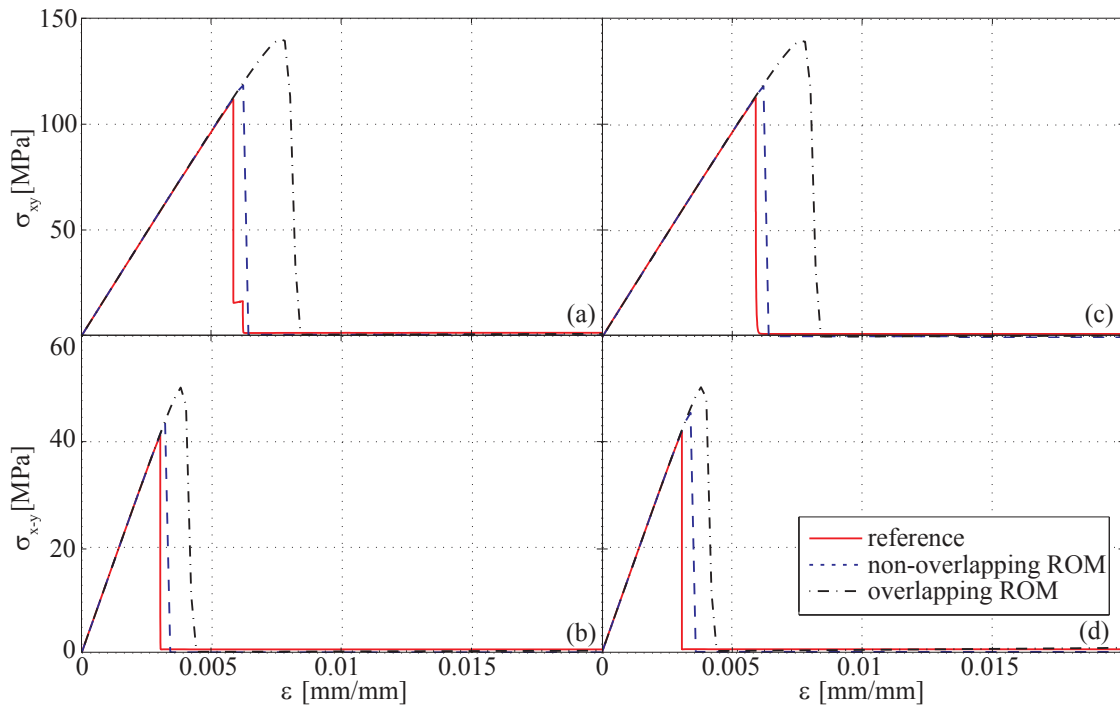


Figure 11: Stress-strain curves when subjected to (a) positive shear loading; (b) negative shear loading; (c) uniaxial in the lateral direction; (d) uniaxial in the vertical direction.

element simulations, the overlapping and non-overlapping ROMs for two normal and shear directions. The ROM simulations shown in this figure do not consider the compatible eigenstrain approach. There are significant post-failure residual stresses in all cases (Fig. 9a-d). In the context of a large multiscale analysis of a component or a structure, the presence of post residual stresses could clearly affect the load redistribution and alter the structural failure characteristics.

Figure 10 illustrates the stress-strain response comparison of the overlapping and non-overlapping ROMs regularized by the compatible eigenstrain method as described in Section 5. The regularized reduced order models demonstrate insignificant post-failure strength for both overlapping and non-overlapping models. The peak strength predicted by the reduced order models slightly over predict that of the reference simulations, but the overall behavior is in reasonable agreement with the reference simulations. Figure 10 also indicates that the non-overlapping ROM with significantly higher model order has nominally better predictions compared to the overlapping ROM. While the overlapping ROM sacrifices some accuracy, it is able to predict the failure behavior reasonably well while solving a smaller set of nonlinear equations. Figure 11 shows the macroscale stress-strain curves for the random cell as computed by the ROMs and the reference simulations. Both ROMs show reasonable agreement with the reference model for each loading scenario. In both ROM cases, the compatible eigenstrains are employed to regularize the post-peak behavior. A significant post-peak stress is observed in the random cell model when not regularized, similar to the cubic cell and the results of the unregularized simulations are omitted for brevity.

## 7 Conclusions

This manuscript provided an improved eigendeformation based reduced order homogenization approach in two key respects. First, the proposed formulation allows the overlapping of the parts (i.e., subdomains) of the microstructure employed in the construction of the reduced order model basis. In the context of the method of failure paths, this capability is essential as the potential failure paths within a microstructure that may activate in various loading conditions may overlap. Second, the presence of spurious residual stresses observed post-failure that occur due to stress locking is alleviated in a computationally efficient manner. A key characteristic of the proposed approach is that the load carrying capacity of the cracked microstructure is retained in the directions transverse to the microcrack. The verification studies performed with particulate composite microstructures with ordered and random configurations point to significant improvements in accuracy, while maintaining a low model order.

## 8 Acknowledgements

The authors gratefully acknowledge the financial support provided by the Aerospace Systems Directorate of the Air Force Research Laboratory (Contract No: GS04T09DBC0017 through Engility Corporation) as well as the graduate fellowship by the Southern Regional Education Board.

## References

- [1] J. Aboudi, S. M. Arnold, and Bednarczyk. B. A. *Micromechanics of Composite Materials. A Generalized Multiscale Analysis Approach*. Elsevier, Amsterdam, 2013.
- [2] I. Babuska. Homogenization and application. mathematical and computational problems. In B. Hubbard, editor, *Numerical Solution of Partial Differential Equations - III, SYNPADE*. Academic Press, 1975.
- [3] Z. P. Bazant and M. Jirasek. Nonlocal integral formulations of plasticity and damage: Survey of progress. *Journal of Engineering Mechanics*, 128:1119–1149, 2002.
- [4] T. B. Belytschko, S. Loehnert, and J. H. Song. Multiscale aggregating discontinuities: a method for circumventing loss of material stability. *Int. J. Numer. Meth. Engng.*, 73: 869–894, 2008.
- [5] A. Benssousan, J. L. Lions, and G. Papanicolaou. *Asymptotic Analysis for Periodic Structures*. North-Holland, Amsterdam, 1978.
- [6] L. V. Berlyand and A. G. Kolpakov. Network approximation in the limit of small interparticle distance of the effective properties of a high-contrast random dispersed composite. *Archive for Rational Mechanics and Analysis*, 159:179–227, 2001.
- [7] S. Bhattacharjee and K. Matous. A nonlinear manifold-based reduced order model for multiscale analysis of heterogeneous hyperelastic materials. *J. Comput. Physics*, 313: 635–653, 2016.
- [8] M. J. Bogdanor and C. Oskay. Prediction of progressive damage and strength of im7/977-3 composites using the eigendeformation-based homogenization approach: Static loading. *J. Composite Mater.*, 2016. doi: 10.1177/0021998316650982.
- [9] M. J. Bogdanor and C. Oskay. Prediction of progressive fatigue damage and failure behavior of im7/977-3 composites using the reduced-order multiple space-time homogenization approach. *J. Composite Mater.*, 2016. doi: 10.1177/0021998316665683.

- [10] M. J. Bogdanor, C. Oskay, and S. B. Clay. Multiscale modeling of failure in composites under model parameter uncertainty. *Comput. Mech.*, 56:389–404, 2015.
- [11] S. Boyaval. Reduced-basis approach for homogenization beyond the periodic setting. *Multiscale Model. Simul.*, 7:466–494, 2008.
- [12] F. Chinesta, A. Ammar, A. Leygue, and Keunings R. An overview of the proper generalized decomposition with applications in computational rheology. *Journal of Non-Newtonian Fluid Mechanics*, 166:578–592, 2011.
- [13] R. Courant and D. Hilbert. *Methods of Mathematical Physics*, volume 1. Wiley-VCH, 1991.
- [14] M. Cremonesi, D. Neron, P. A. Guidault, and P. Ladeveze. A pgd-based homogenization technique for the resolution of nonlinear multiscale problems. *Comput. Meth. Appl. Mech. Engrg.*, 267:275–292, 2013.
- [15] R. Crouch and C. Oskay. Symmetric meso-mechanical model for failure analysis of heterogeneous materials. *Int. J. Mult. Comp. Eng.*, 8:447–461, 2010.
- [16] R. D. Crouch, S. B. Clay, and C. Oskay. Experimental and computational investigation of progressive damage accumulation in cfrp composites. *Compos. Part B: Eng.*, 48:59–67, 2013.
- [17] R. D. Crouch, C. Oskay, and S. B. Clay. Multiple spatio-temporal scale modeling of composites subjected to cyclic loading. *Comp. Mech.*, 51:93–107, 2013.
- [18] G. J. Dvorak. On uniform fields in heterogeneous media. *Proc. R. Soc. Lond. A*, 431:89–110, 1990.
- [19] G. J. Dvorak. Transformation field analysis of inelastic composite materials. *Proc. R. Soc. Lond. A*, 437:311–327, 1992.
- [20] J. Fish and K. L. Shek. Finite deformation plasticity of composite structures: Computational models and adaptive strategies. *Comput. Meth. Appl. Mech. Engrg.*, 172:145–174, 1999.
- [21] J. Fish, K. L. Shek, M. Pandheeradi, and M. S. Shephard. Computational plasticity for composite structures based on mathematical homogenization: Theory and practice. *Comput. Meth. Appl. Mech. Engrg.*, 148:53–73, 1997.

- [22] J. Fish, Q. Yu, and K. L. Shek. Computational damage mechanics for composite materials based on mathematical homogenization. *Int. J. Numer. Meth. Engng.*, 45:1657–1679, 1999.
- [23] J. Fish, V. Filonova, and Z. Yuan. Hybrid impotent-incompatible eigenstrain base homogenization. *Int. J. Numer. Meth. Engng.*, 95:1–32, 2013.
- [24] F. Fritzen and M. Leuschner. Reduced basis hybrid computational homogenization based on a mixed incremental formulation. *Comput. Meth. Appl. Mech. Engrg.*, 260:143–154, 2013.
- [25] R. Furuhashi and T. Mura. On the equivalent inclusion method and impotent eigenstrains. *Journal of Elasticity*, 148:53–73, 1979.
- [26] J. M. Guedes and N. Kikuchi. Preprocessing and postprocessing for materials based on the homogenization method with adaptive finite element methods. *Comput. Meth. Appl. Mech. Engrg.*, 83:143–198, 1990.
- [27] J. A. Hernandez, J. Oliver, A. E. Huespe, M. A. Caicedo, and J. C. Cante. High-performance model reduction techniques in computational multiscale homogenization. *Comput. Meth. Appl. Mech. Engrg.*, 276:149–189, 2014.
- [28] T. Hui and C. Oskay. Computational modeling of polyurea-coated composites subjected to blast loads. *J. Compos. Mater.*, 46:2167–2178, 2012.
- [29] M. Jirasek. Non-local damage mechanics with application to concrete. *Failure, Degradation and Instabilities in Geomaterials*, pages 683–709, 2004.
- [30] V. Kouznetsova, M. G. D. Geers, and W. A. M. Brekelmans. Multi-scale constitutive modelling of heterogeneous materials with a gradient-enhanced computational homogenization scheme. *Int. J. Numer. Meth. Engng.*, 54:1235–1260, 2002.
- [31] H. Lamari, A. Ammar, P. Cartraud, G. Legrain, F. Chinesta, and F. Jacquemin. Routes for efficient computational homogenization of nonlinear materials using the proper generalized decompositions. *Arch. of Comput. Methods in Eng.*, 17:373–391, 2010.
- [32] T. Massart, R. H. J. Peerlings, and M. G. D. Geers. Structural damage analysis of masonry walls using computational homogenization. *Int. J. Damage Mechanics*, 16:199–226, 2007.
- [33] J. Mazars. A description of micro and micro scale damage of concrete structure. *Eng. Fract. Mech.*, 25:729–737, 1986.

- [34] J. C. Michel and P. Suquet. Computational analysis of nonlinear composite structures using the nonuniform transformation field analysis. *Comput. Meth. Appl. Mech. Engng*, 193:5477–5502, 2004.
- [35] M. Mosby and K. Matous. Computational homogenization at extreme scales. *Extreme Mechanics Letters*, 6:68–74, 2016.
- [36] H. Moulinec and P. Suquet. A numerical method for computing the overall response of nonlinear composites with complex microstructure. *Comput. Meth. Appl. Mech. Engng*, 157:69–94, 1998.
- [37] D. Neron and P. Ladeveze. Proper generalized decomposition for multiscale and multiphysics problems. *Arch. of Comput. Methods Eng.*, 17:351–372, 2010.
- [38] V. P. Nguyen, O. Lloberas-Valls, M. Stroeven, and L. J. Sluys. Computational homogenization for multiscale crack modeling implementational and computational aspects. *Int. J. Numer. Meth. Engng.*, 2011. doi: 10.1002/nme.3237.
- [39] C. Oskay. Two-level multiscale enrichment methodology for modeling of heterogeneous plates. *Int. J. Numer. Meth. Engng.*, 80:1143–1170, 2009.
- [40] C. Oskay and J. Fish. Eigendeformation-based reduced order homogenization for failure analysis of heterogeneous materials. *Comp. Meth. Appl. Mech. Engng.*, 196:1216–1243, 2007.
- [41] C. Oskay and J. Fish. On calibration and validation of eigendeformation-based multiscale models for failure analysis of heterogeneous systems. *Comp. Mech.*, 42:181:195, 2008.
- [42] I. Ozdemir, W. A. M. Brekelmans, and M. G. D. Geers.  $\text{Fe}^2$  computational homogenization for thermo-mechanical analysis of heterogeneous solids. *Comp. Meth. Appl. Mech. Engng.*, 198:602–613, 2008.
- [43] G. Pijaudier-Cabot and Z. P. Bazant. Nonlocal damage theory. *ASCE J. Eng. Mech*, 113:1512–1533, 1987.
- [44] E. Sanchez-Palencia. *Non-homogeneous media and vibration theory*, volume 127 of *Lecture Notes in Physics*. Springer-Verlag, Berlin, 1980.
- [45] F. V. Souza, D. H. Allen, and Y. Kim. Multiscale model for predicting damage evolution in composites due to impact loading. *Compos. Sci. Technol.*, 68:2624–2634, 2008.
- [46] P. A. Sparks and C. Oskay. Calibration etc. *Int. J. Numer. Meth. Eng.*, pages 122–156, 2011.

- [47] P. M. Suquet. Elements of homogenization for inelastic solid mechanics. In E. Sanchez-Palencia and A. Zaoui, editors, *Homogenization Techniques for Composite Media*. Springer-Verlag, 1987.
- [48] K. Terada and Kurumatani M. Two-scale diffusion-deformation coupling model for material deterioration involving micro-crack propagation. *Int. J. Numer. Meth. Engng.*, 83: 426–451, 2010.
- [49] K. Terada, I. Saiki, K. Matsui, and Y. Yamakawa. Two-scale kinematics and linearization for simultaneous two-scale analysis of periodic heterogeneous solids at finite strain. *Comput. Methods Appl. Mech. Engng.*, 192:3531–3563, 2003.
- [50] H. Wendland. Piecewise polynomial, positive definite and compactly supported radial functions of minimal degree. *Advances in Comp. Math.*, 4:389–396, 1995.
- [51] H. Yan, C. Oskay, A. Krishnan, and L. R. Xu. Compression after impact response of woven fiber reinforced composites. *Compos. Sci. Technol.*, 70:2128–2136, 2010.
- [52] J. Yvonnet and Q.-C. He. The reduced model multiscale method (R3M) for the non-linear homogenization of hyperelastic media at finite strains. *J. Comput. Phys.*, 223:341–368, 2007. ISSN 0021-9991. doi: 10.1016/j.jcp.2006.09.019.
- [53] X. Zhang and C. Oskay. Eigenstrain based reduced order homogenization for polycrystalline materials. *Comput. Methods Appl. Mech. Engng.*, 297:408–436, 2015.